Robust Retinal Vessel Segmentation via Locally Adaptive Derivative Frames in Orientation Scores

Jiong Zhang*, Behdad Dashtbozorg, Erik Bekkers, Josien P. W. Pluim, *Senior Member, IEEE*, Remco Duits, and Bart M. ter Haar Romeny, *Senior Member, IEEE*

***Abstract*— This paper presents a robust and fully automatic filter-based approach for retinal vessel segmentation. We propose new filters based on 3D rotating frames in so-called orientation scores, which are functions on the Lie-group domain of positions and orientations $\mathbb{R}^2 \rtimes S^1$. By means of a wavelet-type transform, a 2D image is lifted to a 3D orientation score, where elongated structures are disentangled into their corresponding orientation planes. In the lifted domain $\mathbb{R}^2 \rtimes S^1$, vessels are enhanced by means of multi-scale second-order Gaussian derivatives perpendicular to the line structures. More precisely, we use a left-invariant rotating derivative (LID) frame, and a locally adaptive derivative (LAD) frame. The LAD is adaptive to the local line structures and is found by eigensystem analysis of the left-invariant Hessian matrix (computed with the LID). After multi-scale filtering via the LID or LAD in the orientation score domain, the results are projected back to the 2D image plane giving us the enhanced vessels. Then a binary segmentation is obtained through thresholding. The proposed methods are validated on six retinal image datasets with different image types, on which competitive segmentation performances are achieved. In particular, the proposed algorithm of applying the LAD filter on orientation scores (LAD-OS) outperforms most of the state-of-the-art methods. The LAD-OS is capable of dealing with typically difficult cases like crossings, central arterial reflex, closely parallel and tiny vessels. The high computational speed of the proposed methods allows processing of large datasets in a screening setting.**

Manuscript received June 3, 2016; accepted June 28, 2016. Date of publication August 3, 2016; date of current version November 29, 2016. The research leading to these results has received funding from the China Scholarship Council 201206300010. This work is the NWO-H'e Programme of Innovation Cooperation 629.001.003 and the European Foundation for the Study of Diabetes/Chinese Diabetes Society/Lilly project. *Asterisk indicates corresponding author.*

*J. Zhang is with the Department of Biomedical Engineering, Eindhoven University of Technology, 5600 MB Eindhoven, The Netherlands (e-mail: J.Zhang1@tue.nl).

B. Dashtbozorg, E. Bekkers, and J. P. W. Pluim are with the Department of Biomedical Engineering, Eindhoven University of Technology, 5600 MB Eindhoven, The Netherlands (e-mail: B.Dasht.Bozorg@tue.nl; E.J.Bekkers@tue.nl; J.Pluim@tue.nl).

R. Duits is with the Department of Mathematics and Computer Science, and he is also affiliated to the Department of Biomedical Engineering, Eindhoven University of Technology, 5600 MB Eindhoven, The Netherlands (e-mail: R.Duits@tue.nl).

B. M. ter Haar Romeny is with the Department of Biomedical and Information Engineering, Northeastern University, Shenyang 110000, China; he is also with the Department of Biomedical Engineering, Eindhoven University of Technology, 5600 MB Eindhoven, The Netherlands (e-mail: B.M.TerHaarRomeny@tue.nl).

Color versions of one or more of the figures in this paper are available online at http://ieeexplore.ieee.org.

Digital Object Identifier 10.1109/TMI.2016.2587062

***Index Terms*— Gaussian derivatives, orientation scores, retinal image analysis, rotating filter, vessel segmentation.**

I. Introduction

RETINAL fundus images contain rich information about eye-related diseases, such as age-related macular degeneration (AMD), diabetic retinopathy (DR), glaucoma and systemic diseases, such as hypertension and arteriosclerosis [1], and are thus significant for early computer-aided diagnosis and clinical treatment planning.

As part of the blood circulation system, the retinal vessel structure can provide important biomarkers from geometric properties to assist ophthalmologists. The quantitative analysis of retinal vessels requires accurate extraction of the vascular tree from retinal fundus images. However, manual annotations and analysis of the vascular tree by human experts are time consuming and labor intensive due to the vascular complexity. Therefore, the automatic segmentation of retinal vessels is necessary for quantitative analysis. This is a challenging task due to the variations of vessel width, strong central arterial reflex, crossings, highly curved vessel parts, as well as closely parallel and tiny vessels. Hence, a robust and fast vessel segmentation approach to handle difficult cases is particularly needed. Many algorithms have been proposed for retinal vessel segmentation. They can be generally divided into two main categories: supervised methods [2]–[5] and unsupervised methods [6]–[8].

Supervised methods usually give better performance than unsupervised methods since a supervised algorithm learns from given rules to train a classifier which will be used for the discrimination of vessel and non-vessel pixels. The rules are supported by feature vectors extracted from the training samples as input and the manually labeled ground truths as output. Niemeijer *et al.* [9] introduced a feature vector by combing the responses of multi-scale Gaussian matched filters and its derivatives, as well as the green intensity for each pixel, in order to train a model based on a k-Nearest Neighbor (kNN) approach. Moreover, oriented-filters are also considered to set up the feature vectors. Soares *et al.* [2] extracted a feature vector for a Bayesian classifier from the pixel intensity and Gabor filter responses at multiple orientations and scales. One of the best supervised approaches is proposed by Fraz *et al.* [5] which is an ensemble classification system

of boosted and bagged decision trees. The downside of supervised classification is the need for a large number of manually annotated training samples and it is not easy to generalize the trained models to meet the requirements of varying datasets.

Unsupervised methods work without prior knowledge and labeled ground truths, such as tracking-based, model-based and filter-based techniques. Tracking-based methods [6], [10] start from seed points and iteratively expand the connected vessel models to obtain the vascular tree. Bekkers *et al.* [6] proposed an automatic algorithm to track vessel edges through a multi-orientation framework. However, the performance of tracking-based approaches not only heavily relies on the correct initialization of seed points, but also depends on the robustness of the iterative tracking scheme.

Model-based approaches extract vessels by applying explicit vessel profile models [11] or deformable models [12]. The method proposed by Lam *et al.* [11] uses a multi-concavity modeling to process retinal images of both healthy subjects and patients. Al-Diri *et al.* [12] and Zhao *et al.* [13] presented methods for retinal vessel segmentation by applying active contour models.

Other methods [7], [8], [14]–[18], including ours, are based on maximizing filter responses to gray-level profiles of the vessel cross-sections. Compared to supervised methods, these unsupervised methods generally have a higher speed and simpler segmentation process. Mendonça *et al.* [19] proposed differential filters in combination with morphological operators to detect vessel centerlines. The segmentation is obtained using iterative region growing. Zhang *et al.* [17] introduced a generalized matched filter which amplifies the response on the vessel cross-section and reduces the false positives caused by vessel-like structures from pathologies. The recent method presented by Azzopardi *et al.* [8] considers the combination of shifted filter responses (COSFIRE) to detect bar-shaped structures in retinal images. This method is rotation invariant, where the orientation selectivity is determined from given vessel-like structures. Krause *et al.* [16] proposed a retinal vessel segmentation algorithm by convolving the second-order differential operator of the local Radon transform with image data. In this work, we also consider to process image data in a higher-dimensional space, but instead of using the local Radon transform, we rely on the formal group-theoretical framework of orientation scores [20]. Moreover, we exploit the multi-scale vessel segmentation algorithms based on rotation-invariant Gaussian derivatives in the orientation score domain.

The theory of invertible orientation scores is motivated by the orientation-selective property of cortical hypercolumns in the visual cortex [20]. The construction of invertible orientation scores is achieved by lifting 2D images to 3D functions on the roto-translation group $SE(2)$, a Lie-group domain of positions and orientations $\mathbb{R}^2 \rtimes S^1$. By adding a third orientation dimension via the orientation score transform, elongated structures in a 2D image are disentangled into different orientation planes according to their local orientations.

In recent work [21], we set up a routine of applying a rotating filter for enhancing elongated structures in the domain of an orientation score, where a so-called left-invariant rotating derivative (LID) frame is constructed per orientation. The LID frame is aligned with the orientations in the score domain, and it is used for constructing multi-scale LID filters to enhance blood vessels by means of the second-order Gaussian derivative in the perpendicular direction. However, the data alignment with the anisotropic kernel of the orientation score transform will become weak when a low number of orientations is used to construct the score. Thus, the LID frame that is attached to each orientation layer cannot achieve perfect fit to the data in the orientation score domain.

In this paper, in order to achieve full alignment with the local structures in each pixel position and orientation, we build up a new vessel enhancement filter in a locally adaptive derivative (LAD) frame. The LAD frame is constructed via the theory of exponential curve fit in the orientation score domain [22], [23]. Exponential curves are essentially "straight" lines with respect to the curved geometry of $SE(2)$. Via eigensystem analysis of the left-invariant Hessian matrix (obtained using LID), we fit exponential curves that best fit the local (curved) line structures [22].

Using the enhanced image by the multi-scale LAD filters, the vessel segmentation is easily achieved with a high performance by selecting an optimal threshold value. The validation phase demonstrates that the proposed retinal vessel segmentation algorithm not only gives an improved performance on the major parts of the retinal vasculature, but also it is capable of dealing with difficult cases such as strong central reflex, crossings/bifurcations, micro-vessels, closely parallel and highly curved vessel parts.

The contributions of this paper can be summarized as follows.

(i) We proposed a novel retinal vessel segmentation approach based on a simpler version of a 2nd-order locally adaptive derivative. This simpler version performs well in comparison to the state of the art, and it avoids a computation of full Laplacian in vessel enhancements (geometric diffusions) appearing in [22], [23]. Our novel and simple detector, is in our opinion much easier to grasp and reproduce.

(ii) We show that the proposed LAD-OS approach gives good performance even with a small number of orientation sampling, as a consequence of our specific adaptive frame methodology. Compared with the conventional filter-based approaches which usually require large number of orientation samplings, our method is more efficient in computation.

(iii) In addition to the theoretical ideas proposed in this paper, we also give a full evaluation/benchmarking of vessel segmentation via left-invariant processing of orientation scores, which has not been done before. Validations are performed on 6 different datasets with both RGB and SLO retinal image modalities. Experimental results show that the proposed method works robustly on different types of retinal images and gives accurate vessel segmentations.

(iv) The robust and unsupervised approach we proposed is capable of processing both low and high resolution data, which will benefit large-screening programs.

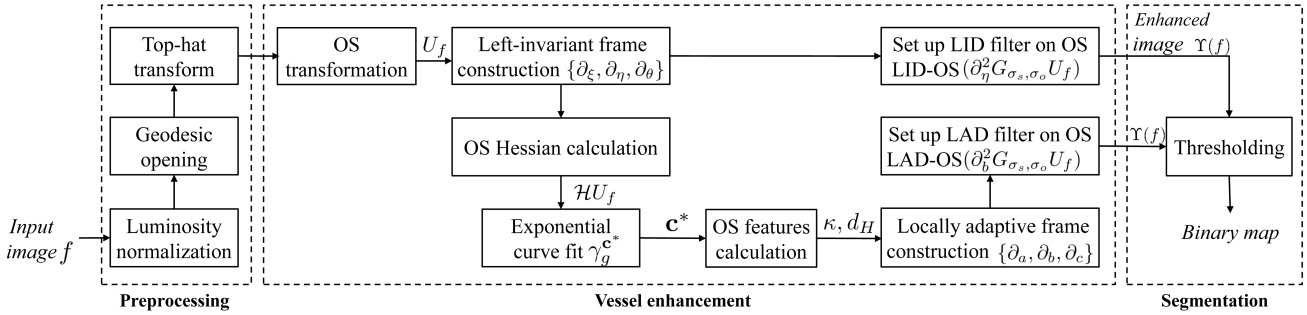

Fig. 1. An overview of our proposed retinal vessel segmentation approaches. OS means orientation score.

TABLE I

EXPLANATIONS OF THE NOTATIONS IN THE METHODOLOGY

Notations	Explanations
$\mathbb{R}^2$	The two-dimensional Euclidean space
$SE(2)$	The Euclidean motion group of planar rotations and translations
$\mathbf{x}$	Spatial variables $(x, y) \in \mathbb{R}^2$ that denote position
θ	Angular variable that denotes orientation
g	$g = (\mathbf{x}, \theta)$ is the group element in $SE(2)$
f	A 2D image
U_f	A 3D orientation score, constructed from image f
$\mathbf{R}_\theta$	A counter-clockwise rotation matrix over angle θ
$\gamma_{SE(2)}$	Curves in SE(2)
$\gamma_{\mathbb{R}^2}$	Plane curves in $\mathbb{R}^2$
t	$t \in \mathbb{R}$ is an arbitrary parameter for defining the arc length of curves
T	A tangent space that is spanned by basis vectors
$\{\partial_\xi, \partial_\eta, \partial_\theta\}$	left-invariant rotating derivative frame of reference
$(c^\xi, c^\eta, c^\theta)$	Vector components expressed in the basis $\{\partial_\xi, \partial_\eta, \partial_\theta\}$
ψ	An anisotropic wavelet kernel
$\mathcal{W}_\psi$	Denoting the transform between image f and orientation score U_f
$\mathbf{c}$	Tangent vector with constant components
$\mathbf{c}^*$	Optimal tangent vector that fits best to the local data
μ	A parameter with physical dimension 1/length to ensure all components are dimensionless
$\mathbf{M}_\mu$	The metric parameterized by μ to determine how the spatial and orientation distances relate to each other
$\mathcal{H}$	The Hessian matrix
κ	The local curvature computed from the optimal tangent vector $\mathbf{c}^*$
d_H	The angle between ∂_ξ and the spatial projection of the tangent vector $\mathbf{c}$
$\{\partial_a, \partial_b, \partial_c\}$	The locally adaptive derivative frame
$\mathbf{Q}_{\kappa,\mu}$	A rotation matrix with rotating over an angle of $\frac{\kappa}{\sqrt{\mu^2+\kappa^2}}$
$\tilde{\mathbf{R}}_{d_H}$	A rotation matrix with rotating over an angle of d_H
Φ	Left-invariant image processing operation on invertible orientation score
Υ	Euclidean-invariant image processing operation on image domain

(v) We show that the proposed method can handle challenging retinal vessel segmentations on which other state-of-the-art methods fail.

(vi) We have published two new type of retinal datasets, the IOSTAR [24] and RC-SLO [25], based on a Scanning Laser Ophthalmoscopy (SLO) technique. To the best of our knowledge, they are the first two publicly available SLO datasets for retinal image analysis.

The paper is organized as follows. In Section II, we describe the geometrical tools and the pipeline for setting up the proposed vessel enhancement filters. Section III presents the proposed vessel segmentation methods. In Section IV, we first describe the experimental datasets with all the settings and measurements. Afterwards, we validate the performance of our methods and compare with the state-of-the-art approaches. Finally, a discussion and conclusion are provided in Section V.

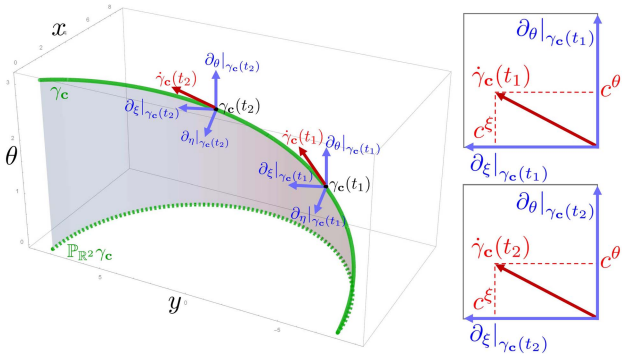

Fig. 2. An exponential curve $\gamma_{\mathbf{c}}$ in the roto-translation group $SE(2)$. Constant tangent vector components $\mathbf{c} = (c^\xi, c^\eta, c^\theta)^T$ are expressed in the left-invariant basis $\{\partial_\xi, \partial_\eta, \partial_\theta\}$.

II. GEOMETRICAL TOOLS FOR VESSEL ENHANCEMENT

In Fig. 1, we summarize the whole routine consisting of three main processing phases: 1) preprocessing, to obtain a uniform illumination distribution and a higher contrast, as well as reduction of strong brightness; 2) vessel enhancement, by maximizing the proposed LID or LAD filter responses of the vessel cross-sections; 3) vessel segmentation, to obtain a binary map by defining a threshold on the enhanced image.

In this section, we will provide the differential geometrical tools for setting up a vessel enhancement approach. We will first give essential explanations of the group theory for understanding the domain $\mathbb{R}^2 \rtimes S^1$, and then we exploit the left-invariant differential operators, tangent vectors, exponential curves and orientation scores in this domain. A notation list is provided in Table I to help the understanding of our methodology.

A. Domain $\mathbb{R}^2 \rtimes S^1 \equiv SE(2)$

The domain $\mathbb{R}^2 \rtimes S^1$ is the coupled space of position and orientations, which can be identified with the roto-translation group $SE(2)$ of planar translations and rotations. The group element on $SE(2)$ is given by $g = (\mathbf{x}, \theta)$, where $\mathbf{x} = (x, y) \in \mathbb{R}^2$ and the group product is given by

$$\begin{aligned} gg' &= (\mathbf{x}, \theta)(\mathbf{x}', \theta') \\ &= (\mathbf{x} + \mathbf{R}_\theta \cdot \mathbf{x}', \theta + \theta'), \quad \textit{for all } g, g' \in SE(2), \end{aligned}$$

where $\mathbf{R}_\theta = \left(\begin{smallmatrix} \cos\theta & -\sin\theta \\ \sin\theta & \cos\theta \end{smallmatrix}\right)$ denotes a counter-clockwise rotation over angle θ. Note that the roto-translation group $SE(2)$ is a non-commutative group, yielding to the property $gg' \neq g'g$ since a rotation matrix $\mathbf{R}_\theta$ pops up in the translation part,

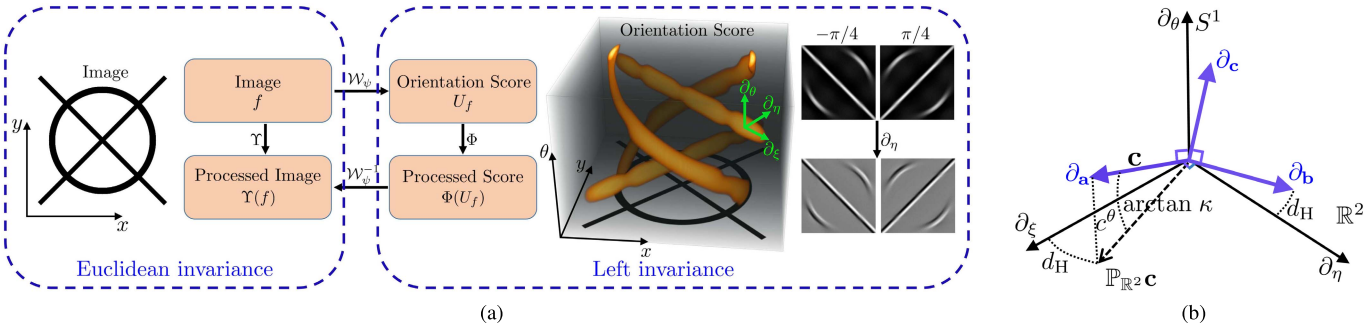

Fig. 3. (a) Transformation from 2D image domain to 3D orientation score on an exemplary image with circle and crossings. Image processing via operators Φ on the invertible orientation score robustly relate to operators Υ on the image domain. Euclidean-invariance of Υ is preserved by left-invariance of Φ. We show the left-invariance property of ∂_η acting on two different orientation layers of the score. (b) The LAD frame $\{\partial_a, \partial_b, \partial_c\}$ is obtained from the LID frame $\{\partial_\xi, \partial_\eta, \partial_\theta\}$ via curvature κ and deviation from horizontality d_{H}.

which is reflected by the *semi*-direct product "$\rtimes$" between $\mathbb{R}^2$ and S^1 [22]. In this work, we are interested in extracting vessel structures, for which the essential differential geometry basics for analyzing locally oriented structures in $SE(2)$ will be explained in the next section.

B. Curves and Tangent Vector Fields in $SE(2)$

1) Curves and Left-Invariant Vector Fields in $SE(2)$: Curves $\gamma_{SE(2)}(t) = (x(t), y(t), \theta(t))^T \in SE(2)$, where $t \in \mathbb{R}$ is an arbitrary parameter for defining the arc length, in the joint space of positions and orientations can be constructed from planar curves $\gamma_{\mathbb{R}^2}(t) = (x(t), y(t))^T \in \mathbb{R}^2$ by adding a third coordinate $\theta(t) = \arg(\dot{x}(t) + i\dot{y}(t))$, i.e. the direction of tangent vectors $\dot{\gamma}_{\mathbb{R}^2}(t) \in T(\mathbb{R}^2)$. Curves in $SE(2)$ that are constructed in such a way are called horizontal curves, and are the natural curves to consider in orientation scores. It is also possible to consider $SE(2)$ curves whose third coordinate does not correspond to the tangent direction of the 2D projections, in which case we say that these curves deviate from horizontality. The planar tangent space $T(\mathbb{R}^2)$ is spanned by the basis[1] $\{\partial_x, \partial_y\}$, and the corresponding tangent space $T(SE(2))$ in the Euclidean motion group $SE(2)$ is spanned by the basis $\{\partial_\xi, \partial_\eta, \partial_\theta\}$. Since in $SE(2)$ we must work with translations over $\mathbf{x}$ and rotations over θ, the tangent space is spanned by the left-invariant rotating derivative (LID) frame of reference that we conveniently denote by

$$\{\partial_\xi, \partial_\eta, \partial_\theta\} := \{\cos\theta\partial_x + \sin\theta\partial_y, \cos\theta\partial_y - \sin\theta\partial_x, \partial_\theta\}, \tag{1}$$

and where throughout this article we use short notation $\partial_x = \frac{\partial}{\partial x}$, $\partial_y = \frac{\partial}{\partial y}$ and $\partial_\theta = \frac{\partial}{\partial \theta}$. See the rotating frames in Fig. 2.

2) Exponential Curves in $SE(2)$: An *exponential curve* is a curve $\gamma_{\mathbf{c}} : \mathbb{R} \to SE(2)$ with constant components $\mathbf{c} = (c^\xi, c^\eta, c^\theta)^T$ of the tangent vector expressed in the left-invariant basis $\{\partial_\xi, \partial_\eta, \partial_\theta\}$, i.e., $\dot{\gamma}_{\mathbf{c}}(t) = c^\xi \partial_\xi|_{\gamma_{\mathbf{c}}(t)} + c^\eta \partial_\eta|_{\gamma_{\mathbf{c}}(t)} + c^\theta \partial_\theta|_{\gamma_{\mathbf{c}}(t)}$, for all $t \in \mathbb{R}$. See Fig. 2. Exponential curves in the curved geometry of $SE(2)$ are similar to *straight lines* in $\mathbb{R}^2$, and provide a local representation of the elongated structures of interest. An exponential curve is constructed by an exponential mapping of the Lie algebra basis. For details see [22], [23], [26]. In this paper, the tangent vectors $\mathbf{c}$ are obtained via the eigensystem analysis of the left-invariant Hessian matrix. This procedure is a form of exponential curve fitting [23] and will be explained in section II-E.

[1]Since vector fields can also be taken as differential operators on smooth and locally defined functions, we write $\{\partial_x, \partial_y\}$ for the basis instead of a more conventional notation $\{\mathbf{e}_x, \mathbf{e}_y\}$ with $\mathbf{e}_x = (1, 0)$ and $\mathbf{e}_y = (0, 1)$.

C. Invertible Orientation Scores on $SE(2)$

The image data is analyzed in the form of orientation scores, which are obtained by lifting 2D images to 3D functions on the roto-translation group $SE(2) = \mathbb{R}^2 \rtimes S^1$. An orientation score $U_f := \mathcal{W}_\psi f$ can be constructed from a 2D image f to an orientation score U_f via wavelet-type transform $\mathcal{W}_\psi$, which is illustrated in Fig. 3a. The transform is achieved through an anisotropic convolution kernel $\psi \in \mathbb{L}_2(\mathbb{R}^2)$:

$$U_f(\mathbf{x}, \theta) = (\mathcal{W}_\psi[f])(\mathbf{x}, \theta) = \int_{\mathbb{R}^2} \overline{\psi(\mathbf{R}_\theta^{-1}(\mathbf{y}-\mathbf{x}))} f(\mathbf{y}) d\mathbf{y}, \tag{2}$$

where in this work we choose cake wavelets [6] for ψ. Cake wavelets are quadrature filters. The real part represents the locally symmetric structures like ridges/lines, while the imaginary part responds to the antisymmetric structures like edges. In the context of vessel filtering in this work, we choose the real-valued cake wavelets.

D. Left-Invariant Operations on Orientation Scores

As shown in Fig. 3a, all left-invariant operations Φ on orientation scores U_f have a strong connection with the Euclidean-invariant operations Υ on the image domain. A desirable property of this relation is that the Euclidean invariance of Υ is ensured by the left-invariance of Φ. In this case, all image processing operations will be invariant with respect to translations and rotations. To this end, the operators Φ on orientation scores need to satisfy $\Phi \circ \mathcal{L}_g = \mathcal{L}_g \circ \Phi$ for all $g \in SE(2)$, with group representation $g \mapsto \mathcal{L}_g$ given by $\mathcal{L}_g U_f(g') = U_f(g^{-1}g') = U_f(R_\theta^{-1}(\mathbf{x}' - \mathbf{x}), \theta' - \theta)$, such that the left-invariance property can be well preserved. Compared with the Cartesian derivative ∂_y in the image domain, the derivative ∂_η is invariant under different orientations in the score domain, and therefore the locally oriented structures can be better preserved after reconstruction to the image domain [27]. In the next section, we will give the pipeline of

extending the LID frame to a locally adaptive derivative (LAD) frame through the exponential curve fit in $SE(2)$.

E. Locally Adaptive Frame From Exponential Curve Fit

The LID frames are aligned with the discrete orientations of the anisotropic kernel used to construct the orientation score. Each orientation layer (corresponding to some θ) thus has its own derivative frame $\{\partial_\xi, \partial_\eta, \partial_\theta\}$. However, the data in the score is not always perfectly aligned with the kernels used to do the lifting, especially when a low number of orientations is used. Hence, we estimate the local orientation (and curvature) by means of second-order exponential curve fits (part 1), and re-align the LID frames accordingly (part 2 and 3).

1) Optimal Tangent Vector $\mathbf{c}^*(g)$ for Exponential Curve Fit: Where in flat Euclidean spaces one can estimate the direction of oriented structures by locally fitting straight lines, we do the same in $SE(2)$. However, now "straight" is defined with respect to the curved geometry of $SE(2)$, and the straight curves are known as exponential curves. Here, we compute exponential curves that locally best fit the data, and use the optimal tangent vectors $\mathbf{c}^*$ to define the LAD frame. More precisely, we find tangent vectors $\mathbf{c}^*$ of best fit exponential curves by solving the following minimization problem:

$$\mathbf{c}^*(g) = \underset{\mathbf{c}\in\mathbb{R}^3, ||\mathbf{c}||_\mu=1}{\operatorname{argmin}} \left\{ ||\frac{d}{dt}\nabla U_f(\gamma_g^{\mathbf{c}}(t))|_{t=0}||_\mu^2 \right\}, \tag{3}$$

with $||\mathbf{c}||_\mu^2 = \mu^2|c^\xi|^2 + \mu^2|c^\eta|^2 + |c^\theta|^2 = ||\mathbf{M}_\mu \mathbf{c}||^2$, where $\mathbf{M}_\mu = \operatorname{diag}(\mu, \mu, 1)$ and an intrinsic parameter μ is used to balance spatial and orientation distances. μ has dimension [1/length], and makes that length quantities are dimensionless. In (3) we effectively minimize the gradient magnitude along exponential curve fits. To solve (3) we first rewrite it using

$$\begin{aligned}\mathcal{E}(\mathbf{c}) &:= ||\frac{d}{dt}\nabla U_f(\gamma_g^{\mathbf{c}}(t))|_{t=0}||_\mu^2 \\ &= \mathbf{c}^T(\mathcal{H}U_f(g))^T \mathbf{M}_{\mu^{-2}} \mathcal{H}U_f(g)\mathbf{c},\end{aligned} \tag{4}$$

where $\nabla U_f = \mathbf{M}_{\mu^{-2}}(\partial_\xi U_f, \partial_\eta U_f, \partial_\theta U_f)^T$, and $\mathcal{H}U_f$ represents the Hessian matrix in the orientation score domain which is computed via the left-invariant derivative frame $\{\partial_\xi, \partial_\eta, \partial_\theta\}$:

$$\mathcal{H}U_f = \begin{pmatrix} \partial_\xi^2 U_f & \partial_\xi\partial_\eta U_f & \partial_\theta\partial_\xi U_f \\ \partial_\xi\partial_\eta U_f & \partial_\eta^2 U_f & \partial_\theta\partial_\eta U_f \\ \partial_\xi\partial_\theta U_f & \partial_\eta\partial_\theta U_f & \partial_\theta^2 U_f \end{pmatrix}. \tag{5}$$

Then by substituting (5) in (3), and using the Euler-Lagrange technique we obtain the following minimizing condition:

$$\begin{aligned}\nabla\mathcal{E}(\mathbf{c}^*) &= \lambda\nabla(||\mathbf{c}^*||_\mu^2 - 1), \\ (\mathcal{H}U_f)^T \mathbf{M}_{\mu^{-2}}(\mathcal{H}U_f)\mathbf{c}^* &= \lambda \mathbf{M}_{\mu^2}\mathbf{c}^*, \\ (\mathcal{H}_\mu U_f)\tilde{\mathbf{c}}^* &= \lambda\tilde{\mathbf{c}}^*,\end{aligned} \tag{6}$$

with $\mathbf{c}^* = \operatorname{argmin}\{\mathcal{E}(\mathbf{c}) \mid \|\mathbf{c}\|_\mu = 1)\}$, and with $\mathcal{H}_\mu U_f = \mathbf{M}_{\mu^{-1}}(\mathcal{H}U_f)^T\mathbf{M}_{\mu^{-2}}(\mathcal{H}U_f)\mathbf{M}_{\mu^{-1}}$ the symmetrized[2] and μ normalized left invariant Hessian, and $\tilde{\mathbf{c}}^* = \mathbf{M}_\mu\mathbf{c}^*$. The eigenvectors of $\mathcal{H}_\mu U_f$ solve (6), and it is the eigenvector with lowest eigenvalue that solves (3). The just described curve fitting procedure results in 2nd order exponential curve fits. For other methods for fitting exponential curves, and for more details regarding external regularization we refer to [22], [23], [26].

2) Local Curvature κ and Deviation From Horizontality d_H: From the tangent vector $\mathbf{c}^*$ of the exponential curve fit, we can directly compute local curvature κ and deviation from horizontality[3] d_H [22] via

$$\kappa = \frac{c^\theta \operatorname{sign}(c^\xi)}{\sqrt{(c^\eta)^2 + (c^\xi)^2}}, \qquad d_{\mathrm{H}} = \arctan\left(\frac{c^\eta}{c^\xi}\right). \tag{7}$$

As shown in Fig. 3b, d_H represents the angle between ∂_ξ and the projection $\mathbb{P}_{\mathbb{R}^2}\mathbf{c}$ of the tangent vector $\mathbf{c}$ on $\mathbb{R}^2$.

3) Locally Adaptive Derivative (LAD) Frame $\{\partial_a, \partial_b, \partial_c\}$: By considering both κ and d_{H}, obtained via the 2nd order local exponential curve fits, we can rotate the left-invariant derivative frame via two rotations $\tilde{\mathbf{R}}_{d_{\mathrm{H}}}$ and $\mathbf{Q}_{\kappa,\mu}$, as shown in Fig. 4, in order to obtain the locally adaptive derivative frame $\{\partial_a, \partial_b, \partial_c\}$:

$$\begin{pmatrix} \partial_a \\ \partial_b \\ \partial_c \end{pmatrix} = \mathbf{Q}_{\kappa,\mu}^T \tilde{\mathbf{R}}_{d_{\mathrm{H}}}^T \begin{pmatrix} \partial_\xi \\ \partial_\eta \\ \mu\partial_\theta \end{pmatrix}, \tag{8}$$

where

$$\begin{aligned}\tilde{\mathbf{R}}_{d_{\mathrm{H}}} &= \begin{pmatrix} \cos d_{\mathrm{H}} & -\sin d_{\mathrm{H}} & 0 \\ \sin d_{\mathrm{H}} & \cos d_{\mathrm{H}} & 0 \\ 0 & 0 & 1 \end{pmatrix}, \\ \mathbf{Q}_{\kappa,\mu} &= \begin{pmatrix} \frac{\mu}{\sqrt{\mu^2+\kappa^2}} & 0 & \frac{\kappa}{\sqrt{\mu^2+\kappa^2}} \\ 0 & 1 & 0 \\ \frac{-\kappa}{\sqrt{\mu^2+\kappa^2}} & 0 & \frac{\mu}{\sqrt{\mu^2+\kappa^2}} \end{pmatrix}.\end{aligned} \tag{9}$$

In our final vessel enhancement pipeline (Fig. 4), the vessels are enhanced via second-order derivatives ∂_b (in the direction perpendicular to the vessels). An important efficiency consideration here is that, once the left-invariant Hessian $\mathcal{H}U_f$ and the $\{\partial_a, \partial_b, \partial_c\}$ frame are computed, the ∂_b^2 derivatives can be efficiently computed by projecting the Hessian matrix onto the direction vector $\mathbf{e}_b$ (recall footnote 1) via

$$\partial_b^2 U_f = \mathbf{e}_b^T(\mathcal{H}U_f)\mathbf{e}_b. \tag{10}$$

F. Left-Invariant Gaussian Derivatives on Orientation Scores

It is well known that the second-order differential operators/filters can be used to obtain high responses on elongated structures like vessel profiles [14], [16]. In this section, we are going to construct the rotating filters for vessel enhancement via the second-order Gaussian derivatives in both the LID frame $\{\partial_\xi, \partial_\eta, \partial_\theta\}$ and the LAD frame $\{\partial_a, \partial_b, \partial_c\}$.

Suitable linear or non-linear combinations of derivatives in different orders have been widely used in applications of geometric structure/feature detections, e.g. edge, ridge and corner detection. However, directly taking derivatives on discrete data is an ill-posed problem. In order to preserve the well-posedness

[2]Note that the Hessian in Eq. (5) is not symmetric, due to the non-commutative group structure, i.e $\partial_\theta\partial_\xi U_f \neq \partial_\xi\partial_\theta U_f$.

[3]Horizontality of a lifted curve means that $\theta(t) = \arctan(\dot{x}(t)+\dot{y}(t))$, which essentially means that $c^\eta = 0$ for horizontal curves.

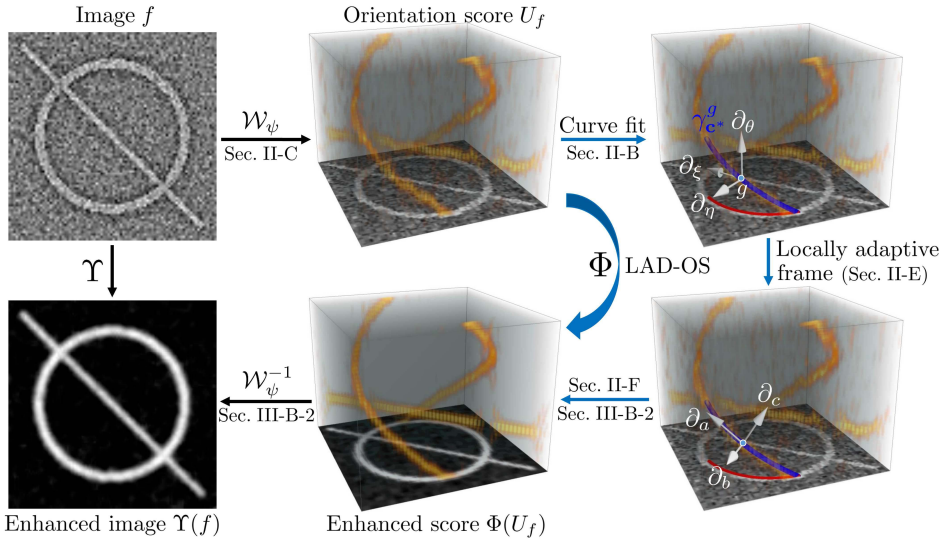

Fig. 4. The whole routine of achieving elongated structure enhancement operation Υ via left-invariant operation Φ based on the locally adaptive frame $\{\partial_a, \partial_b, \partial_c\}$. The exponential curve fit from $\{\partial_\xi, \partial_\eta, \partial_\theta\}$ to $\{\partial_a, \partial_b, \partial_c\}$ provides full alignment with local structures.

TABLE II

THE CORRESPONDING PARAMETERS FOR EACH DATASET THAT ARE AUTOMATICALLY DEFINED DURING THE WHOLE PROCEDURE

Datasets	Image size (px)	FOV	Pixel size $\rho \sim \mu m/px$	Vessel caliber Mean $\pm$ SD (px)	*Preprocessing* W_l (px)	*Preprocessing* W_t (px)	*Vessel enhancement* *No*	*Vessel enhancement* S	*Vessel enhancement* σ_o LID	*Vessel enhancement* σ_o LAD	*Segmentation* *MCC*	*Segmentation* T_h
DRIVE	565×584	45°	27	3.4 ± 1.6	19	6	16	$\{0.7, 1.0, 1.5, ..., 4.5\}$	$\pi/5$	$\pi/40$	0.7571	0.5540
STARE	700×605	35°	17	4.4 ± 2.6	29	9	16	$\{0.7, 1.0, 1.5, ..., 4.5\}$	$\pi/5$	$\pi/40$	0.7558	0.5940
CHASE_DB1	999×960	30°	10	5.4 ± 3.6	50	15	16	$\{2, 3.5, 4.5, ..., 8.5\}$	$\pi/5$	$\pi/40$	0.7030	0.6160
HRF	3504×2336	45°	4	8.7 ± 5.9	125	37	16	$\{2, 3, 4, ..., 10\}$	$\pi/5$	$\pi/40$	0.7410	0.6100
IOSTAR	1024×1024	45°	14	6.3 ± 2.5	36	11	16	$\{2, 3, 4, ..., 8\}$	$\pi/5$	$\pi/40$	0.7318	0.6100
RC-SLO	360×320	45°	14	5.2 ± 2.5	36	11	16	$\{2, 3, 4, ..., 8\}$	$\pi/5$	$\pi/40$	0.7327	0.6080

of left-invariant operators, we construct the regularized orientation scores via convolutions with *spatially isotropic* Gaussian kernels $G_{\sigma_s,\sigma_o}(\mathbf{x},\theta) = G_{\sigma_s}(\mathbf{x})G_{\sigma_o}(\theta)$, with a $d-$dimensional Gaussian given by $G_\sigma(\mathbf{x}) = (2\pi\sigma^2)^{-d/2}\, e^{-\frac{\|\mathbf{x}\|^2}{2\sigma^2}}$, and where $\sigma_s > 0$ and $\sigma_o > 0$ provide the 2D-spatial scale $\frac{1}{2}\sigma_s^2$ and 1D-angular scale $\frac{1}{2}\sigma_o^2$ of the Gaussian kernel. The multi-scale Gaussian derivatives in orientation scores are applied to pick up geometric structures according to their varying widths.

III. VESSEL SEGMENTATION

A. Preprocessing

Since the green channel of retinal images in RGB datasets has better contrast between the vessels and the background [2], [9], [15], [19], [28], we will only use the green channel for our experiments. Retinal image quality often suffers from non-uniform illumination and varying contrast, which will influence the performance of subsequent vessel segmentation. Therefore, the luminosity normalization technique proposed by Foracchia *et al.* [29] is employed to obtain a uniform illumination distribution. Moreover, a geodesic opening and a morphological top-hat transform are used to reduce the erroneous detection caused by the brightness of the optic disk and central reflections, as well as to improve the contrast between foreground and background. In order to automatically determine the preprocessing parameters, we define the luminosity normalization window size W_l and the top-hat transform kernel size W_t equal to 500 μm and 150 μm, respectively. In each dataset, the window size in pixels is obtained by dividing W_l and W_t by the image physical pixel size ρ, as shown in Table II.

B. Vessel Enhancement Derivative Filters

1) Method 1: Left-Invariant Derivative (LID) Filter on Orientation Scores (LID-OS): In this section, the multi-scale second-order Gaussian derivatives based on the local coordinates system $\{\xi, \eta, \theta\}$ in the orientations score domain, are employed as operators/filters to enhance vessel profiles [14], [16]. In order to achieve a high response on a vessel cross-section, we construct a rotating filter that is perpendicular to the local orientation θ of the elongated structures. As shown in Fig. 3a and 4, such a vessel-enhancing filter Φ can be obtained via the left-invariant rotating operator $\partial_\eta = -\sin\theta\partial_x + \cos\theta\partial_y$ on the orientation scores. Therefore, by considering the second-order Gaussian derivatives in the LID frame $\{\partial_\xi, \partial_\eta, \partial_\theta\}$, we propose the second-order operator $\Phi_\eta^{\sigma_s,\sigma_o}(U_f) := -\partial_\eta^2 G_{\sigma_s,\sigma_o} * U_f$, named as LID filter, for vessel enhancement.

By applying the LID filter directly on orientation scores, the responses on vessel parts are heightened in each

orientation layer. Since elongated structures are disentangled into different orientation planes separately in the score domain, the proposed rotating LID filter is capable of enhancing and preserving complex crossings/bifurcations.

In this work we keep the filter responses dimensionless and truly scale-invariant by setting the scale normalization factor $\mu = \sigma_o/\sigma_s$. The angular blurring σ_o is set as a small constant over all spatial scales σ_s such that the extrema filter responses can be still consistent. Moreover, the conversion factor μ with physical unit 1/length is also used here to balance the orientation and spatial direction that have different units. Here we achieve the scale-normalization via $\mu^{-2} = \sigma_s^2/\sigma_o^2$ for our second-order LID filter [21] that is given by

$$\Phi^{\sigma_s,\sigma_o}_{\eta,\text{norm}}(U_f) := \mu^{-2}\Phi^{\sigma_s,\sigma_o}_{\eta}(U_f) = -\mu^{-2}\partial^2_{\eta} G_{\sigma_s,\sigma_o} * U_f, \tag{11}$$

from which we will obtain the multi-scale filtered orientation scores. The final image reconstruction from the multi-scale filtered orientation scores is obtained via

$$\Upsilon(f)(\mathbf{x}) := \max_{\theta_i \in \frac{\pi}{No}\{1,\ldots,No\}} \left\{ \sum_{\sigma_s \in \mathcal{S}} \Phi^{\sigma_s,\sigma_o}_{\eta,\text{norm}}(U_f)(\mathbf{x},\theta_i) \right\}, \tag{12}$$

where No and $\mathcal{S}$ represent the number of orientations and the spatial scalings respectively, $\theta_i = i\frac{\pi}{No}$, and the maximum filter response is calculated over all orientations per position.

2) Method 2: Locally Adaptive Derivative (LAD) Filter on Orientation Scores (LAD-OS): Based on the LID frame $\{\partial_\xi, \partial_\eta, \partial_\theta\}$ on each orientation, we obtain the multi-scale rotating LID filters for vessel enhancement. However, since this frame is only defined globally for each orientation plane rather than locally for each pixel in the score domain, the LID filters are not always aligned perfectly with all local orientations. We have to take into account a large number of orientation samplings No such that all elongated structures of different orientations can be enhanced in the LID frame.

Following the theory of exponential curve fit as described in Sub Section II-E, we set up the LAD frame $\{\partial_a, \partial_b, \partial_c\}$ which is adaptive to each position and orientation of the data. Subsequently, our proposed LAD filter can be constructed via the second-order Gaussian derivatives $\Phi^{\sigma_s,\sigma_o}_{b}(U_f) := -\partial^2_b G_{\sigma_s,\sigma_o} * U_f$ at multiple scales in the orientation score domain. Compared with the LID filter, the newly proposed LAD provides perfect alignment to local structures, and therefore it is more robust to orientation changes, and even allows to use a small number of orientations. The scale-normalized LAD filter can be written as

$$\begin{aligned}\Phi^{\sigma_s,\sigma_o}_{b,\text{norm}}(U_f) &:= \mu^{-2}\Phi^{\sigma_s,\sigma_o}_{b}(U_f) \\ &= -\mu^{-2}\partial^2_b G_{\sigma_s,\sigma_o} * U_f. \end{aligned} \tag{13}$$

The final image reconstruction from the multi-scale filtered orientation scores is given by

$$\Upsilon(f)(\mathbf{x}) := \max_{\theta_i \in \frac{\pi}{No}\{1,\ldots,No\}} \left\{ \sum_{\sigma_s \in \mathcal{S}} \Phi^{\sigma_s,\sigma_o}_{b,\text{norm}}(U_f)(\mathbf{x},\theta_i) \right\}, \tag{14}$$

C. Hard Segmentation

After applying the proposed LID or LAD filters on the orientation scores of a retinal image, the vessel part will be enhanced showing high filter responses, while the background part will be suppressed showing low responses. By rescaling the enhanced image between 0 and 1 and setting a suitable threshold value T_h, an enhanced image is segmented into a binary map with only vessel pixels and non-vessel pixels.

IV. Validation and Experimental Results

A. Material

In this work, four established publicly available color retinal fundus datasets DRIVE [28], STARE [7], CHASE_DB1 [30] and the High-Resolution Fundus dataset HRF [31] and our two newly public IOSTAR [24] and RC-SLO [25] (RetinaCheck - Scanning Laser Ophthalmoscopy) datasets are used for evaluating the proposed vessel enhancement filters.

The DRIVE dataset [28] contains 40 color retinal fundus images (divided into test and training sets, and each of which contains 20 images) with a resolution of 565×584 pixels. For each image, the vascular tree is annotated by two human observers. The performance of the segmentation algorithms are evaluated on the test set. The STARE dataset [7] includes 20 color fundus images with a resolution of 700×605 pixels, in which 10 images contain pathologies. Two groups of manually segmented binary maps are provided by two observers. The CHASE_DB1 dataset [30] contains 28 color retinal fundus images with a resolution of 999×960 pixels, acquired from both the left and right eye of 14 child subjects. All the images are also manually annotated by two human observers. The public High-Resolution Fundus (HRF) image dataset [31] has 45 images with division into three groups: healthy, glaucoma and diabetic retinopathy, each of which has 15 images. All the images have a resolution of 3504×2336 pixels.

In addition to the RGB fundus images, we also provide two public datasets, the IOSTAR [24] and the RC-SLO [25] datasets with a different image modality. The images in these two datasets are acquired with an EasyScan camera (i-Optics Inc., the Netherlands), which is based on a Scanning Laser Ophthalmoscopy (SLO) technique. The IOSTAR dataset includes 30 images with a resolution of 1024×1024 pixels and the RC-SLO dataset contains 40 image patches with a resolution of 360×320 pixels. All the vessels in both datasets are annotated by a group of experts working in the field of retinal image analysis. The RC-SLO dataset covers a wide range of difficult cases, such as high curvature changes, central vessel reflex, micro-vessels, crossings/bifurcations.

All the measurements in this work are computed by considering all the pixels within the Field of View (FOV). The FOV masks of the DRIVE and HRF datasets are respectively provided by their authors and the ones of the CHASH_DB1, STARE, IOSTAR and RC-SLO datasets are created manually since the FOV boundary in the retinal image is obvious.

B. Performance Measurements

To compare the binary segmentation results with their corresponding manual ground truths, we obtain the following four performance measurements: the vessel pixels in the ground truth that are correctly classified as vessels in the segmentation results are denoted as true positives (TP). If they are labeled as non-vessels, they are considered as false negatives (FN). The non-vessel pixels in the ground truth that are correctly classified as non-vessels in the segmentation results are denoted as true negatives (TN). If they are predicted as vessels, they are counted as false positives (FP).

To make a global performance comparison of the proposed algorithm with state-of-the-art vessel segmentation methods, we evaluate the performance measures: *Sensitivity* (*Se*), *Specificity* (*Sp*), *Accuracy* (*Acc*). There metrics are given by

$$Se = \frac{\mathrm{TP}}{\mathrm{TP}+\mathrm{FN}}, \quad Sp = \frac{\mathrm{TN}}{\mathrm{TN}+\mathrm{FP}}, \quad Acc = \frac{\mathrm{TP}+\mathrm{TN}}{\mathrm{N}},$$

where $\mathrm{N} = \mathrm{TN} + \mathrm{TP} + \mathrm{FN} + \mathrm{FP}$.

The *Matthews correlation coefficient* (*MCC*) is often used in the quality measurement of a binary classification system for two classes with different sizes. In the case of retinal vessel segmentation, only a small portion of pixels belongs to the vessels (only around 9%-14% vessel pixels), while the others are counted as background pixels. Therefore, the defined *MCC* value can be used to find the optimal system settings for a vessel segmentation algorithm. The *MCC* is defined as $MCC = (\mathrm{TP/N\text{-}S} \times \mathrm{P})/(\sqrt{\mathrm{P} \times \mathrm{S} \times (1-\mathrm{S}) \times (1-\mathrm{P})})$ where $\mathrm{S} = (\mathrm{TP}+\mathrm{FN})/\mathrm{N}$ and $\mathrm{P} = (\mathrm{TP}+\mathrm{FP})/\mathrm{N}$.

In order to evaluate the quality of our vessel enhancement results, the receiving operator characteristics (ROC) curve is computed with the true positive ratio (*Se*) versus the false positive ratio ($1 - Sp$) with respect to the varying threshold value T_h. The area under the ROC curve (AUC) is calculated to quantify the performance of the segmentation, where the AUC value 1 represents a perfect segmentation. As shown in Fig. 7, an algorithm will have a better performance if its corresponding ROC curve is closer to the top-left corner.

C. Settings

In order to easily generalize the proposed method to different data, the parameters are primarily defined based on the physical properties of each dataset separately. As shown in Table II, the main parameters of the proposed method are determined from the image properties, such as the image size, FOV and physical pixel size ρ, which are determined by the specifications of the fundus camera. Since we explore the second-order Gaussian derivatives to construct the proposed filters for vessel enhancement, the spatial scale samplings $\mathcal{S}$ are determined by looking at the filter windows that can enhance the vessel profiles best. By considering the average vessel caliber of each dataset in Table II, we can roughly estimate the spatial scale samplings which can give us relatively the best performance for our experiments. In our experiments, we use 7 scales for the DRIVE, STARE, CHASE_DB1, IOSTAR and RC-SLO datasets, and we use 9 scales for the HRF dataset due to its high resolution.

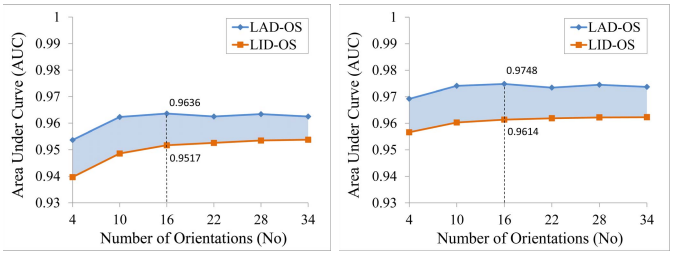

Fig. 5. Area under curve (AUC) comparisons of the two proposed vessel enhancement filters with respect to different number of orientations for the (a) DRIVE and (b) STARE datasets.

It is worth mentioning that adding more scales will not improve the global performance too much. Moreover, a small angular blurring σ_o is set to keep structure smoothness, and we set the same number of orientations *No* in all the experiments for the wavelets transform.

For the purpose of conducting a global evaluation on different datasets, e.g. the measurement of sensitivity, specificity and accuracy, we need an optimized threshold to obtain the binary segmentation on the probability map. The best threshold value T_h for each dataset is selected based on the one at which we can achieve the highest *MCC* value. All the threshold values T_h are shown in Table II and the corresponding global performance measures of our proposed methods obtained with *MCC* on the three public datasets are shown in Table III.

D. Vessel Enhancement Based on the LID and LAD Filters

In this section, the vessel segmentation performance based on the two proposed filters will be evaluated on the public retinal image datasets DRIVE and STARE by the two following routines: *1)* multi-scale LID filters on orientation scores (LID-OS) for vessel segmentation, and *2)* multi-scale LAD filters on orientation scores (LAD-OS).

In Fig. 5, the AUC value of each approach is calculated as a measure for describing the segmentation performance. Since the alignment of each proposed vessel enhancement filter to local structures is influenced by the number of wavelet orientations, we will evaluate their segmentation performance with different orientation samplings *No*. The locally adaptive property of the LAD filter provides perfect alignment with local structures, so it is able to achieve a higher and more robust performance with respect to varying orientation discretization compared to the LID filter. Even with only 4 orientations, the LAD-OS approach is able to reach the AUC values of 0.9537 and 0.9692, compared to 0.9538 and 0.9623 of the LID-OS approach with 34 orientations on the DRIVE and STARE datasets, respectively. In Fig. 6, we show examples of applying the LID-OS and LAD-OS on a typical image patch with the interference of central reflex, curvature changes and low intensities on tiny vessels. Since the LAD frame is adapted to align the local structure by taking into account the neighborhood pixels via eigensystem analysis of the Hessian matrix, the contextual information is better included to reduce the inference from the central reflex. The curved segments of tiny vessels are also better preserved through the local

TABLE III
SEGMENTATION RESULTS ON THE DRIVE, STARE AND CHASE_ DB1 DATASETS

			DRIVE				STARE				CHASE_DB1			
	Methods	Year	*Se*	*Sp*	*Acc*	AUC	*Se*	*Sp*	*Acc*	AUC	*Se*	*Sp*	*Acc*	AUC
	2nd human observer	-	0.7760	0.9724	0.9472	-	0.8952	0.9384	0.9349	-	0.8105	0.9711	0.9545	-
Unsupervised methods	Mendonça [19]	2006	0.7344	0.9764	0.9452	-	0.6996	0.9730	0.9440	-	-	-	-	-
	Martinez-Perez [35]	2007	0.7246	0.9655	0.9344	-	0.7506	0.9569	0.9410	-	-	-	-	-
	Al-Diri [12]	2009	0.7282	0.9551	-	-	0.7521	0.9681	-	-	-	-	-	-
	Lam [11]	2010	-	-	0.9472	0.9614	-	-	0.9567⋆	0.9739	-	-	-	-
	Zhang [17]	2010	0.7120	0.9724	0.9382	-	0.7177	0.9753	0.9484	-	-	-	-	-
	You [36]	2011	0.7410	0.9751	0.9434	-	0.7260	0.9756	0.9497	-	-	-	-	-
	Fraz [37]	2012	0.7152	0.9759	0.9430	-	0.7311	0.9680	0.9442	-	-	-	-	-
	Roychowdhury [32]	2015	0.7395	0.9782	0.9494⋆	0.9672⋆	0.7317	0.9842⋆	0.9560	0.9673	0.7615	0.9575	0.9467⋆	0.9623⋆
	Azzopardi [8]	2015	0.7655	0.9704	0.9442	0.9614	0.7716	0.9701	0.9497	0.9563	0.7585	0.9587	0.9387	0.9487
	Yin [38]	2015	0.7246	0.9790⋆	0.9403	-	0.8541⋆	0.9419	0.9325	-	-	-	-	-
	Proposed LID-OS	2016	**0.7473**	**0.9764**	**0.9474**	**0.9517**	**0.7676**	**0.9764**	**0.9546**	**0.9614**	**0.7562**	**0.9675⋆**	**0.9457**	**0.9565**
	Proposed LAD-OS	2016	**0.7743⋆**	**0.9725**	**0.9476**	**0.9636**	**0.7791†**	**0.9758**	**0.9554**	**0.9748⋆**	**0.7626⋆†**	**0.9661**	**0.9452**	**0.9606**
Supervised methods	Niemeijer [9]	2004	-	-	0.9416	0.9294	-	-	-	-	-	-	-	-
	Staal [28]	2004	-	-	0.9441	0.9520	-	-	0.9516	0.9614	-	-	-	-
	Soares [2]	2006	0.7332	0.9782	0.9466	0.9614	0.7207	0.9747	0.9480	0.9671	-	-	-	-
	Ricci [15]	2007	-	-	0.9595	0.9558	-	-	0.9584	0.9602	-	-	-	-
	Lupascu [3]	2010	0.7200	-	0.9597†	0.9561	-	-	-	-	-	-	-	-
	Marin [4]	2011	0.7067	0.9801	0.9452	0.9588	0.6944	0.9819	0.9526	0.9769	-	-	-	-
	Fraz [5]	2012	0.7406	0.9807	0.9480	0.9747†	0.7548	0.9763	0.9534	0.9768	0.7224	0.9711	0.9469	0.9712
	Orlando [39]	2016	0.7897†	0.9684	-	-	0.7680	0.9738	-	-	0.7277	0.9712	-	-
	Li [40]	2016	0.7569	0.9816†	0.9527	0.9738	0.7726	0.9844†	0.9628†	0.9879†	0.7507	0.9793†	0.9581†	0.9716†

⋆ Best values in comparison with the unsupervised methods; † Best values in comparison with the supervised methods.

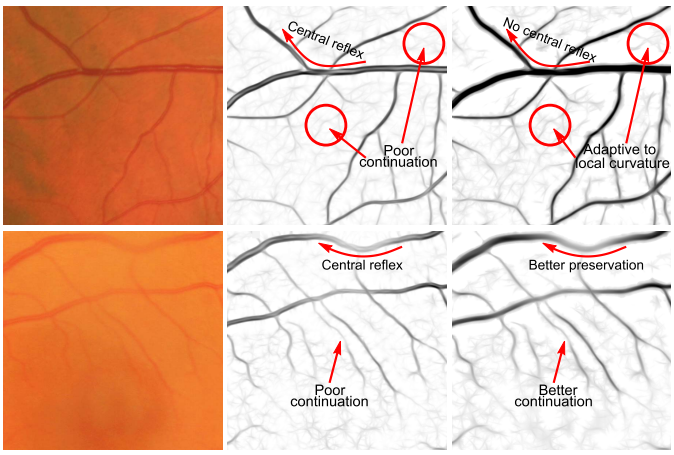

(a) Original patch (b) LID-OS (c) LAD-OS

Fig. 6. Examples of segmentation in the presence of central vessel reflex and tiny structures using the proposed LID-OS and LAD-OS with the same preprocessing step and scale samplings. (a) the original patch, (b) the probability map from the LID-OS and (c) the probability map from the LAD-OS. The curved arrows indicate the central reflex along vessels.

adaptivity property. We can observe that the LAD-OS is more tolerant to strong central reflex and is better at producing high contrast between vessels and background compared to the LID-OS.

In the following experiments, the LAD-OS approach will be adopted with the parameter settings as shown in Table II to obtain the segmentation results. Qualitative and quantitative analysis are performed based on those results.

E. Vessel Segmentation Results of the LAD-OS Algorithm

In Fig. 7, we show the ROC curves for the DRIVE, STARE and CHASE_DB1 datasets. The performance of the 2nd human observer and our proposed LAD-OS algorithm are represented by green squares and blue stars, respectively. For the sake of comparison, the performance of some recently proposed methods are also depicted in this figure. The performance obtained from the 2nd human observer is very close to our ROC curves or located on them.

TABLE IV
SEGMENTATION RESULTS ON THE HRF, IOSTAR AND RC-SLO DATASETS

Methods	Datasets	Year	*Se*	*Sp*	*Acc*	AUC	*MCC*
Odstrcilik [31]	HRF	2013	0.7794	0.9650	0.9494	-	0.7065
Orlando [39]	HRF	2016	0.7874	0.9584	-	-	0.6897
LAD-OS	HRF	2016	**0.7978**	**0.9717**	**0.9556**	**0.9608**	**0.7410**
LAD-OS	IOSTAR	2016	**0.7545**	**0.9740**	**0.9514**	**0.9615**	**0.7318**
LAD-OS	RC-SLO	2016	**0.7787**	**0.9710**	**0.9512**	**0.9626**	**0.7327**

Fig. 8 shows examples of vessel segmentation results of the 6 datasets. We also show the ground truth images that were annotated by the first human observer as references. We can see that our proposed LAD-OS approach is able to preserve most of the small vessel structures, which has great clinical significance for the assessment of biomarkers like fractal dimension (complexity of the vasculature) [33] and detection of neovascularization (formation of new microvasculature) [34]. To compare with the state-of-the-art vessel segmentation algorithms, we evaluate the proposed methods with the performance metrics *Se*, *Sp*, *Acc* and AUC for the DRIVE, STARE, CHASE_DB1 and HRF datasets as shown in Table III, and Table IV. The performance measurements, particularly *Acc* and AUC values demonstrate that the proposed LAD-OS method outperforms most of the unsupervised

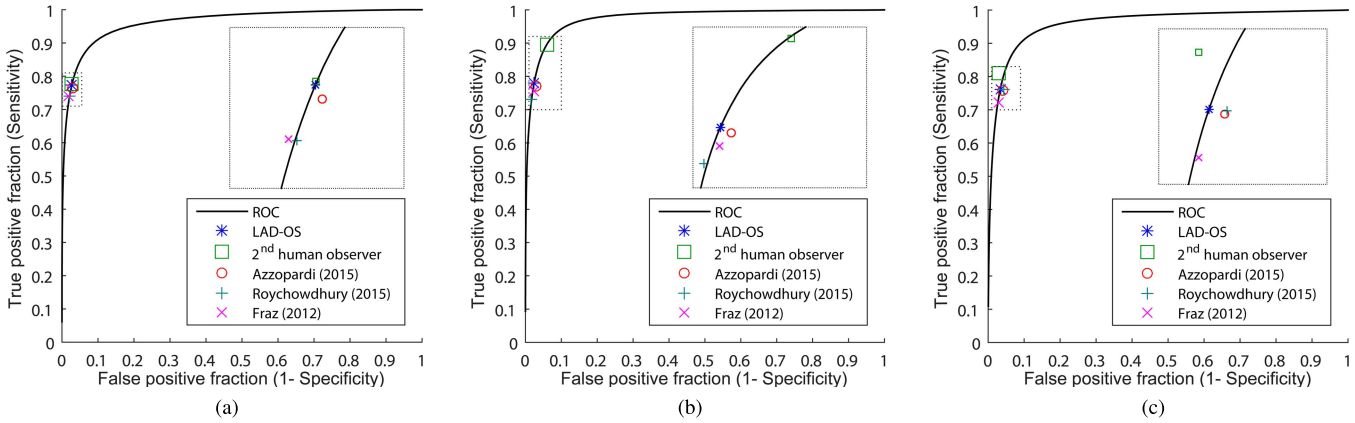

Fig. 7. ROC curves of our proposed LAD-OS approach for the (a) DRIVE, (b) STARE and (c) CHASE_DB1 datasets. Comparisons with the 2nd human observer, the supervised method by Fraz *et al.* [5], the unsupervised methods by Azzopardi *et al.* [8] and Roychowdhury *et al.* [32] are shown in the figure.

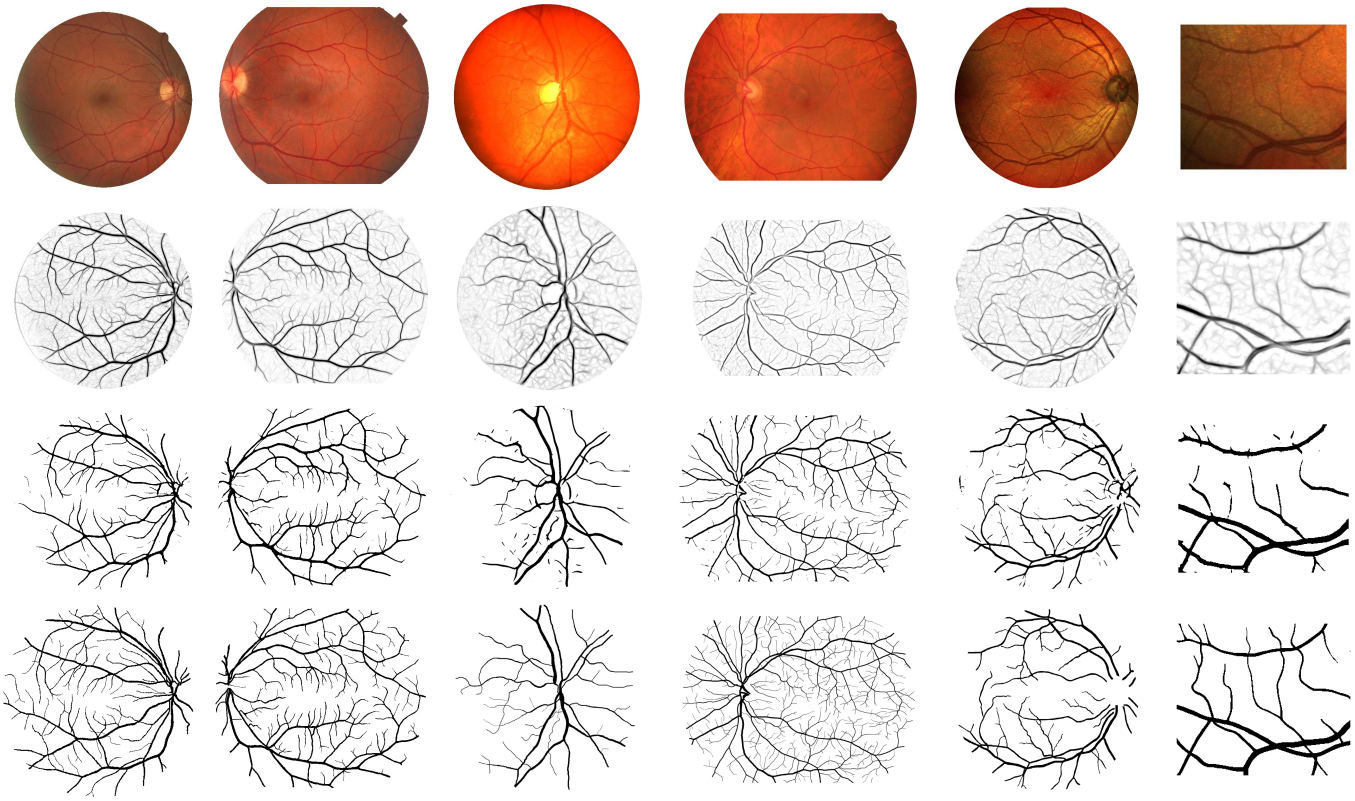

Fig. 8. Examples of vessel segmentation by the proposed LAD-OS approach on images from the 6 datasets. From Row 1 to 4: original color images, vessel enhancement, hard segmentation and manual segmentation results. (a) An image from the DRIVE dataset ($Se = 0.8329$, $Sp = 0.9834$, $Acc = 0.9656$ and $MCC = 0.8324$). (b) An image from the STARE dataset ($Se = 0.8317$, $Sp = 0.9792$, $Acc = 0.9609$ and $MCC = 0.8181$). (c) An image from the CHASE_DB1 dataset ($Se = 0.8643$, $Sp = 0.9623$, $Acc = 0.9546$ and $MCC = 0.7319$). (d) An image from the HRF dataset ($Se = 0.7935$, $Sp = 0.9711$, $Acc = 0.9537$ and $MCC = 0.7449$). (e) An image from the IOSTAR dataset ($Se = 0.8516$, $Sp = 0.9719$, $Acc = 0.9590$ and $MCC = 0.7940$). (f) An image from the RC-SLO dataset ($Se = 0.8190$, $Sp = 0.9692$, $Acc = 0.9490$ and $MCC = 0.7824$).

and supervised methods on all the 6 color fundus image datasets. The results on the HRF dataset show that the proposed LAD-OS approach is able to handle high-resolution data.

F. Evaluation on the Scanning Laser Ophthalmoscopy Images

Color fundus images are extensively used in the evaluation of the state-of-the-art retinal vessel segmentation algorithms. In this paper, the proposed LAD-OS approach is also applied on both the IOSTAR and RC-SLO datasets with SLO images and it achieves very good performance as shown in Table IV. In Fig. 8, we show examples of vessel segmentation that are automatically obtained by the proposed LAD-OS algorithm on an IOSTAR image and a RC-SLO image with difficult cases like micro-vessels, crossings and closely parallel vessels.

V. Discussion and Conclusion

In this work, we firstly proposed the LID filter which is constructed based on the left-invariant rotating derivative frame $\{\partial_\xi, \partial_\eta, \partial_\theta\}$ in the Euclidean roto-translation group $SE(2)$. The LID filter is then applied on orientation scores, i.e. data that is obtained by lifting 2D images to 3D functions on $SE(2)$, to enhance elongated structures. One important advantage of orientation scores is that elongated structures, like lines in crossings and bifurcations are disentangled into their corresponding orientation planes. Consequently, complex structures can be enhanced by the proposed LID-OS routine with a crossing-preserving manner.

However, the LID filter is not always aligned perfectly with local structures in the score domain, especially when the orientation resolution is small. To solve this problem, the LAD filter is obtained by eigensystem analysis of the left-invariant Hessian matrix, which is computed via the LID rotating frame. Since this LAD filter is capable of providing full alignment with local structures on multiple scales in the score domain, the filter responses can be enhanced on elongated structures accurately. Therefore, the proposed LAD-OS approach can be exploited to segment vessels in different applications.

A. Results Overview

The ROC curves in Fig. 5 shows that the supervised method proposed by Fraz *et al.* [5] performs slightly better than our method on the DRIVE dataset, while our proposed method outperforms both the method by Fraz *et al.* [5] and the unsupervised approach by Azzopardi *et al.* [8] on the STARE and CHASE_DB1 datasets. The performance of the unsupervised method by Roychowdhury *et al.* [32] is similar as our method on the DRIVE and STARE datasets, while our proposed LAD-OS approach outperforms all the other ones on the CHASE_DB1 dataset.

Considering the performance of the LAD-OS method on the DRIVE, STARE and CHASE_DB1 datasets, the obtained results outperform most of the state-of-the-art unsupervised and supervised algorithms. Compared to the *Se* and *Sp* (0.7655 and 0.9704 for the DRIVE, 0.7716 and 0.9701 for the STARE, and 0.7585 and 0.9587 for the CHASE_DB1) of one of the best unsupervised approaches by Azzopardi *et al.* [8], the proposed LAD-OS can respectively reach better sensitivity of 0.7858, 0.8481 and 0.8037 at the same specificity level along the ROC curves (Fig. 7). Also the LID-OS algorithm can obtain the sensitivity 0.7702, 0.7969 and 0.7958, respectively for the DRIVE, STARE and CHASE_DB1 at the same specificity.

Compared with the supervised approaches, the proposed LAD-OS method achieves similar or better results, as shown in Fig. 7 and Table III. For the STARE and CHASE_DB1 datasets, we get higher sensitivity of 0.7791 and 0.7371 than one of the best supervised methods by Fraz *et al.* [5] with sensitivity of 0.7548 and 0.7224 at the same specificity level, respectively. For the DRIVE dataset, Fraz's method obtains slightly better result with sensitivity of 0.7406 than LAD-OS with sensitivity of 0.7284 at the same specificity of 0.9807 along the ROC curve. Nevertheless, as shown in Fig. 7 our results are very close to the 2nd observer. In Table IV, the performance of the LAD-OS approach on the high-resolution HRF dataset reaches a sensitivity of 0.8442 compared with the sensitivity of 0.7874 reported by Orlando *et al.* [39] at the same specificity level of 0.9584. Additionally, the evaluation results of our method on the SLO images achieve the AUC of 0.9615 and 0.9626, respectively, on the IOSTAR and RC-SLO datasets, thus demonstrating the robustness of the LAD-OS on different image modalities. The LAD-OS vessel segmentation method is an unsupervised technique, which does not rely on any labor-intensive training phase, but is still able to achieve similar performance compared to the most recently proposed supervised algorithms.

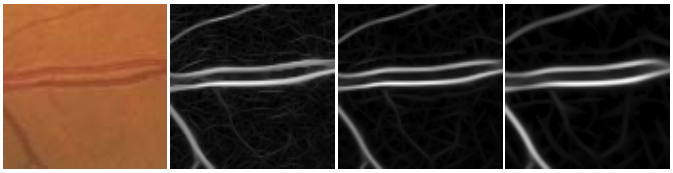

(a) Original patch (b) Scale 0.7 px (c) Scale 1.5 px (d) Scale 2.5 px

Fig. 9. Examples of applying the multi-scale LAD filter at scales 0.7 px, 1.5 px and 2.5 px on an image patch with closely parallel vessels from the low resolution DRIVE dataset.

B. Performance Analysis on Challenging Cases

Structures with strong central reflex, micro-vessels, crossings/bifurcations, closely parallel or highly curved vessel parts are the generally challenging cases in retinal vessel segmentation. To deal with central light reflex, we employ the bottom-hat transform and geodesic opening as a preprocessing step. This also reduces the strong brightness from the optic disk. Besides that, the second-order LAD frame is designed to align with the local structure and exploit much better the notion of context. By using the fully aligned LAD operator, the whole vessel profiles can be better enhanced without suffering too much from the central vessel reflex.

To deal with the wide range of vessel calibers, we designed the multi-scale vessel-enhancing LAD filters with proper scale samplings. Here the set of scales were defined by considering the typical vessel caliber distributions of retinal fundus images. The orientation score transform itself picks up elongated structures of all scales due to the fact that the Fourier kernel covers all the frequencies. 2D elongated structures with different scales like crossings/bifurcations are thus lifted to the 3D orientation score space, where they are separated from each other based on orientations without any information loss and scale selection. Micro-vessels, crossings and bifurcations are well-preserved after 2D reconstruction from multi-scale processing of orientation scores.

Also the problem of parallel blood vessels is dealt with correctly by means of multi-scale processing with an appropriate set of scales. Our LAD filter in the orientation score domain employs spatially isotropic blurring σ_s on each orientation plane and an additionally small angular blurring σ_o to keep structure smoothness along the vessel directions, which leads to fewer artifacts even with very small scales. Fig. 9 shows the

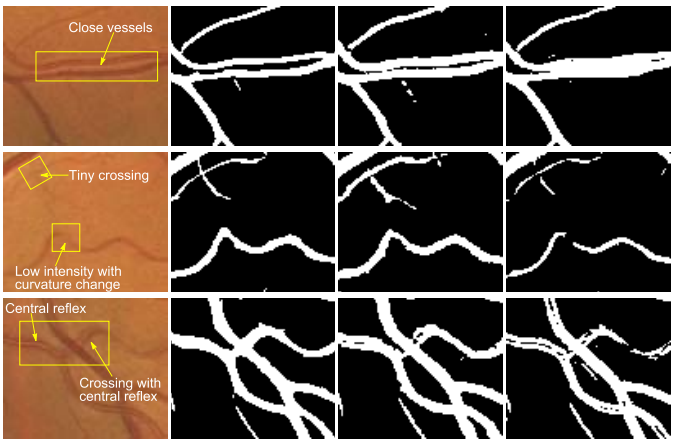

(a) Original Image (b) LAD-OS (c) Azzopardi *et al.* (c) Soares *et al.*

Fig. 10. Comparisons of vessel segmentation results on difficult cases.

probability maps of different scale samplings of the proposed method on two vessels that are close together.

The proposed LAD filter has the good property of alignment with each locally present oriented structure. The local curvature κ and deviation from horizontality d_H are used to optimize the tangent vector $\mathbf{c}^*$ and construct the LAD frame. Hence, our LAD filter is more robust to local curvature changes along the curvilinear structures.

Fig. 10 shows some examples where the recently proposed B-COSFIRE filter [8] and the supervised segmentation by Soares *et al.* [2] fail in the cases of micro-crossing and central reflex. Soares's method also presents merging of closely parallel vessels. This is probably due to the fact that a large portion of the training samples is located on large trunks rather than small branchings in retinal vessels. The trained classifier will have a tendency to treat two parallel vessels as one large vessel. Nevertheless, the LAD-OS algorithm is able to preserve those difficult structures, indicating the ability for providing a more accurate vascular tree.

C. Contributions to Differential Invariant Theory in SE(2) and Its Applications

Previous work [22], [23] provides the theoretical formulation of the locally adaptive derivative frame. There they consider the case of applying crossing-preserving flows for left-invariant diffusions. In this work, we consider different differential invariants for designing vessel-enhancing filters. Compared to the full Laplacian (in cross-sectional b-c plane obtained in Eq. (8)) that is used in [22], [23] to find the maximum eigenvectors, our method proposes a much simpler way by directly taking the spatial part (b direction) of the 2nd order differential operators. The high performance of our application demonstrates that the full Laplacian is not necessarily needed. In addition to the theoretical ideas proposed in our method, this is also the first time where our novel detectors (as explained in the previous item) are included in a full retinal vessel segmentation framework with extensive comparisons to the complete state-of-the-art algorithms. These points were not addressed in previous works. In fact, this study shows that for medical imaging applications like vessel segmentation in retinal images, it is beneficial to further explore geometric reasoning by adaptive left-invariant derivative operators in position and orientation space.

TABLE V
AVERAGE TIME FOR PROCESSING ONE IMAGE

Type	Methods	Year	Running time
Unsupervised methods	**LAD-OS**	2016	20 s
	LID-OS	2016	4 s
	Azzopardi [8]	2015	10 s
	Al-Diri [12]	2009	11 min
	Mendonça [19]	2006	2.5 min
Supervised methods	Li [40]	2016	1.2 min
	Fraz [5]	2012	2 min
	Marin [4]	2011	1.5 min
	Soares [2]	2006	27.5 s

D. Speed Comparison and Parameter Settings

The main computational cost of our method depends on the numbers of orientations and scales in the filtering process. The proposed vessel segmentation routines can achieve a competitive running time with sufficient orientations and scales. Using *Mathematica 10.2* with a computer of 2.7 GHz CPU, the time requirement for segmenting a retinal image in the DRIVE dataset is about 20 seconds and 4 seconds for the LAD-OS and LID-OS algorithms, respectively. The computational efficiency can be further improved by optimizing the implementation of our algorithms. We give a running time comparison in Table V to show the potential of applying our proposed methods on large datasets in a screening setting. For a fair comparison, we recalculate the computational cost of Soares' method [2] on the same PC configuration using Matlab R2015a, and we take the execution time of other recently published approaches from their corresponding publications.

The main parameters for our proposed vessel enhancement techniques are the number of orientations (No) in the wavelet transformation, the spatial scale samplings S and angular scale σ_o shown in Table II. All parameters we used in the proposed algorithms are defined with respect to the physical pixel size and the estimated vessel calibers. Therefore, our methods can be easily generalized for different datasets to obtain reliable vessel segmentation results.

E. Application Scope

Based on the vessel segmentation results of our method, we can also extract different biomarkers like fractal dimension, curvature, vessel width, bifurcation/crossing angles and use them for clinical analysis. Besides that, the proposed method can be further applied on other types of medical images for extracting elongated structures. In Fig. 11, we show the application of applying our method on corneal nerve fiber segmentation.

Although the proposed LAD-OS approach shows very good performance, there are still some limitations in our method that need to be solved in future work. Since our method

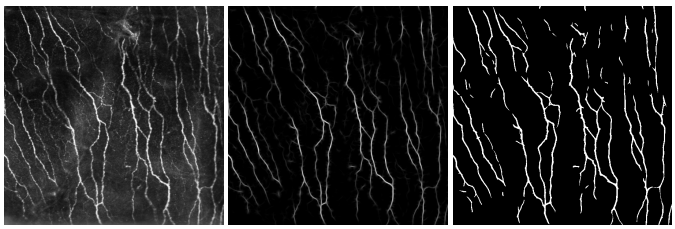

(a) Original patch (b) Enhanced patch (c) Binary map

Fig. 11. Examples of applying the proposed LAD-OS segmentation approach on a patch of an image with corneal nerve fibers.

is able to enhance vessel-like cross-sections, false detections of dark profiles between two bright exudate regions may happen when processing pathological images. These false positives can either be reduced by including a preprocessing or postprocessing step, or by integrating shape information of the vessel cross-section into vessel filtering, which can help to distinguish the differences between vessel and pathological profiles as in [17].

F. Conclusion

In this paper, we have proposed a robust, fast and unsupervised filtered-based algorithm for retinal vessel segmentation. Different from the conventional filters in the 2D image domain, we set up the LID-OS and LAD-OS approaches by considering the left-invariant rotating derivative frame and its extension to the locally adaptive derivative frame in orientation scores. The validation results on 6 different types of datasets show that the LAD-OS filter not only gives more robust and accurate results compared with most of the state-of-the-art segmentation schemes, but also deals with difficult vessel geometries. The high computational efficiency gives the potential of applying the proposed methods on large datasets.

ACKNOWLEDGMENT

The authors would like to thank the international groups for kindly making available their benchmark datasets and annotations. The authors would like to acknowledge Dr. Gonzalo Sanguinetti (TU/e) and MSc. Michiel Janssen (TU/e) for the fruitful discussions. The authors also thank to Dr. Jan Schouten and his colleagues for providing the image with corneal nerve fibers. The authors appreciate the valuable suggestions and comments from the anonymous reviewers.

REFERENCES

[1] M. D. Abràmoff, M. K. Garvin, and M. Sonka, "Retinal imaging and image analysis," Jan., *IEEE Rev. Biomed. Eng.*, vol. 3, no. 1, pp. 169–208, 2010.

[2] J. V. B. Soares, J. J. G. Leandro, R. M. Cesar, H. F. Jelinek, and M. J. Cree, "Retinal vessel segmentation using the 2-D Gabor wavelet and supervised classification," *IEEE Trans. Med. Imag.*, vol. 25, no. 9, pp. 1214–1222, Sep. 2006.

[3] C. A. Lupaşcu, D. Tegolo, and E. Trucco, "FABC: Retinal vessel segmentation using AdaBoost," *IEEE Trans. Inf. Technol. Biomed.*, vol. 14, no. 5, pp. 1267–1274, Sep. 2010.

[4] D. Marín, A. Aquino, M. E. Gegúndez-Arias, and J. M. Bravo, "A new supervised method for blood vessel segmentation in retinal images by using gray-level and moment invariants-based features," *IEEE Trans. Med. Imag.*, vol. 30, no. 1, pp. 146–158, Jan. 2011.

[5] M. M. Fraz *et al.*, "An ensemble classification-based approach applied to retinal blood vessel segmentation," *IEEE Trans. Biomed. Eng.*, vol. 59, no. 9, pp. 2538–2548, Sep. 2012.

[6] E. Bekkers, R. Duits, T. Berendschot, and B. ter Haar Romeny, "A multi-orientation analysis approach to retinal vessel tracking," *J. Math. Imag. Vis.*, vol. 49, no. 3, pp. 583–610, 2014.

[7] A. D. Hoover, V. Kouznetsova, and M. Goldbaum, "Locating blood vessels in retinal images by piecewise threshold probing of a matched filter response," *IEEE Trans. Med. Imag.*, vol. 19, no. 3, pp. 203–210, Mar. 2000.

[8] G. Azzopardi, N. Strisciuglio, M. Vento, and N. Petkov, "Trainable COSFIRE filters for vessel delineation with application to retinal images," *Med. Image Anal.*, vol. 19, no. 1, pp. 46–57, 2015.

[9] M. Niemeijer, J. Staal, B. van Ginneken, M. Loog, and M. D. Abramoff, "Comparative study of retinal vessel segmentation methods on a new publicly available database," *Proc. SPIE*, vol. 5370, pp. 648–656, May 2004.

[10] Y. Yin, M. Adel, and S. Bourennane, "Retinal vessel segmentation using a probabilistic tracking method," *Pattern Recognit.*, vol. 45, no. 4, pp. 1235–1244, 2012.

[11] B. S. Lam, Y. Gao, and A. W.-C. Liew, "General retinal vessel segmentation using regularization-based multiconcavity modeling," *IEEE Trans. Med. Imag.*, vol. 29, no. 7, pp. 1369–1381, Jul. 2010.

[12] B. Al-Diri, A. Hunter, and D. Steel, "An active contour model for segmenting and measuring retinal vessels," *IEEE Trans. Med. Imag.*, vol. 28, no. 9, pp. 1488–1497, Sep. 2009.

[13] Y. Zhao, L. Rada, K. Chen, S. P. Harding, and Y. Zheng, "Automated vessel segmentation using infinite perimeter active contour model with hybrid region information with application to retinal images," *IEEE Trans. Med. Imag.*, vol. 34, no. 9, pp. 1797–1807, Sep. 2015.

[14] A. Frangi, W. Niessen, K. Vincken, and M. Viergever, "Multiscale vessel enhancement filtering," in *Medical Image Computing and Computer-Assisted Intervention*. New York: Springer, 1998, pp. 130–137.

[15] E. Ricci and R. Perfetti, "Retinal blood vessel segmentation using line operators and support vector classification," *IEEE Trans. Med. Imag.*, vol. 26, no. 10, pp. 1357–1365, Oct. 2007.

[16] M. Krause, R. M. Alles, B. Burgeth, and J. Weickert, "Fast retinal vessel analysis," *J. Real-Time Image Process.*, vol. 11, no. 2, pp. 413–422, 2013.

[17] B. Zhang, L. Zhang, L. Zhang, and F. Karray, "Retinal vessel extraction by matched filter with first-order derivative of Gaussian," *Comput. Biol. Med.*, vol. 40, no. 4, pp. 438–445, 2010.

[18] J. Hannink, R. Duits, and E. Bekkers, "Crossing-preserving multi-scale vesselness," in *Medical Image Computing and Computer-Assisted Intervention*. New York: Springer, 2014, pp. 603–610.

[19] A. Mendonça and A. Campilho, "Segmentation of retinal blood vessels by combining the detection of centerlines and morphological reconstruction," *IEEE Trans. Med. Imag.*, vol. 25, no. 9, pp. 1200–1213, Sep. 2006.

[20] R. Duits, M. Felsberg, G. Granlund, and B. ter Haar Romeny, "Image analysis and reconstruction using a wavelet transform constructed from a reducible representation of the Euclidean motion group," *Int. J. Comput. Vis.*, vol. 72, no. 1, pp. 79–102, 2007.

[21] J. Zhang, E. Bekkers, S. Abbasi, B. Dashtbozorg, and B. ter Haar Romeny, "Robust and fast vessel segmentation via Gaussian derivatives in orientation scores," in *Image Analysis Process.*, vol. 9279, Manuscript revised, 2015., pp. 537–547.

[22] E. Franken and R. Duits, "Crossing-preserving coherence-enhancing diffusion on invertible orientation scores," *Int. J. Comput. Vis.*, vol. 85, no. 3, pp. 253–278, 2009.

[23] R. Duits and E. Franken, "Left-invariant parabolic evolutions on SE (2) and contour enhancement via invertible orientation scores. Part II: Nonlinear left-invariant diffusions on invertible orientation scores," *Q. Appl. Math.*, vol. 68, no. 2, pp. 293–331, 2010.

[24] (2015). *IOSTAR Dataset*. [Online]. Available: www.retinacheck.org

[25] (2015). *RC-SLO Dataset*. [Online]. Available: www.retinacheck.org

[26] R. Duits, M. H. J. Janssen, J. Hannink, and G. R. Sanguinetti, "Locally adaptive frames in the roto-translation group and their applications in medical imaging," *J. Math. Imag. Vis.*, pp. 1–36, Mar. 2016.

[27] J. Zhang, R. Duits, G. Sanguinetti, and B. M. ter Haar Romeny, "Numerical approaches for linear left-invariant diffusions on SE (2), their comparison to exact solutions, and their applications in retinal imaging," *Numer. Math. Theor. Methods Appl.*, vol. 9, no. 1, pp. 1–50, 2016.

[28] J. Staal, M. D. Abràmoff, M. Niemeijer, M. Viergever, and B. Van Ginneken, "Ridge-based vessel segmentation in color images of the retina," *IEEE Trans. Med. Imag.*, vol. 23, no. 4, pp. 501–509, Apr. 2004.

[29] M. Foracchia, E. Grisan, and A. Ruggeri, "Luminosity and contrast normalization in retinal images," *Med. Image Anal.*, vol. 9, no. 3, pp. 179–190, 2005.

[30] C. G. Owen *et al.*, "Measuring retinal vessel tortuosity in 10-year-old children: Validation of the computer-assisted image analysis of the retina (CAIAR) program," *Invest. Ophthalmol. Vis. Sci.*, vol. 50, no. 5, pp. 2004–2010, 2009.

[31] J. Odstrcilik *et al.*, "Retinal vessel segmentation by improved matched filtering: Evaluation on a new high-resolution fundus image database," *IET Image Process.*, vol. 7, no. 4, pp. 373–383, Jun. 2013.

[32] S. Roychowdhury, D. D. Koozekanani, and K. K. Parhi, "Iterative vessel segmentation of fundus images," *IEEE Trans. Biomed. Eng.*, vol. 62, no. 7, pp. 1738–1749, Jul. 2015.

[33] N. Patton *et al.*, "Retinal image analysis: Concepts, applications and potential," *Prog. Retinal Eye Res.*, vol. 25, no. 1, pp. 99–127, 2006.

[34] J. Lee, B. C. Y. Zee, and Q. Li, "Detection of neovascularization based on fractal and texture analysis with interaction effects in diabetic retinopathy," *PLoS ONE*, vol. 8, no. 12, p. e75699, 2013.

[35] M. Martinez-Perez, A. Hughes, S. Thom, A. Bharath, and K. Parker, "Segmentation of blood vessels from red-free and fluorescein retinal images," *Med. Image Anal.*, vol. 11, no. 1, pp. 47–61, 2007.

[36] X. You, Q. Peng, Y. Yuan, Y.-M. Cheung, and J. Lei, "Segmentation of retinal blood vessels using the radial projection and semi-supervised approach," *Pattern Recognit.*, vol. 44, no. 10, pp. 2314–2324, 2011.

[37] M. M. Fraz *et al.*, "An approach to localize the retinal blood vessels using bit planes and centerline detection," *Comput. Methods Programs Biomed.*, vol. 108, no. 2, pp. 600–616, 2012.

[38] B. Yin *et al.*, "Vessel extraction from non-fluorescein fundus images using orientation-aware detector," *Med. Image Anal.*, vol. 26, no. 1, pp. 232–242, 2015.

[39] J. Orlando, E. Prokofyeva, and M. Blaschko, "A discriminatively trained fully connected conditional random field model for blood vessel segmentation in fundus images," *IEEE Trans. Biomed. Eng.*, to be published.

[40] Q. Li *et al.*, "A cross-modality learning approach for vessel segmentation in retinal images," *IEEE Trans. Med. Imag.*, vol. 35, no. 1, pp. 109–118, Jan. 2016.